

Metasurface of strongly coupled excitons and plasmonic arrays

Farsane Tabataba-Vakili,^{1,2} Lukas Krelle,^{1,3} Lukas Husel,¹ Huy P. G. Nguyen,¹ Zhijie Li,¹ Ismail Bilgin,¹ Kenji Watanabe,⁴ Takashi Taniguchi,⁵ and Alexander Högele^{1,2}

¹*Fakultät für Physik, Munich Quantum Center, and Center for NanoScience (CeNS), Ludwig-Maximilians-Universität München, Geschwister-Scholl-Platz 1, 80539 München, Germany*

²*Munich Center for Quantum Science and Technology (MCQST), Schellingstraße 4, 80799 München, Germany*

³*Now at: Institute for Condensed Matter Physics,*

Technische Universität Darmstadt, Hochschulstraße 6, 64289 Darmstadt, Germany

⁴*Research Center for Functional Materials, National Institute for Materials Science, 1-1 Namiki, Tsukuba 305-0044, Japan*

⁵*International Center for Materials Nanoarchitectonics,*

National Institute for Materials Science, 1-1 Namiki, Tsukuba 305-0044, Japan

(Dated: February 15, 2024)

Metasurfaces allow to manipulate light at the nanoscale with planar lenses and holograms as prominent applications. Integrating metasurfaces with transition metal dichalcogenide monolayers provides additional functionality to ultrathin optics, such as tunable optical properties and enhanced light-matter interaction. Here, we developed a novel fabrication method that allows to directly integrate such a monolayer with a plasmonic lattice without compromising optical quality or coupling strength, by embedding the gold nanodisk array into an encapsulating hBN layer. We demonstrate plasmon-exciton-polaritons in this metasurface with a large Rabi splitting and strongly modified polarization and emission characteristics, as compared to a bare monolayer, achieving narrow-angle, directional, linearly polarized emission.

Ultrathin optical components known as metasurfaces have the potential to strongly impact modern optics by offering new functionality and unprecedented compactness. Comprised of periodic arrays of sub-wavelength nanostructures, metasurfaces modulate the amplitude, phase, or polarization of incident light [1–3]. Plasmonic metasurfaces consisting of metallic nanostructures provide strong field enhancement and have been used to introduce abrupt phase changes [4], create holograms [5], and realize ultrathin lenses [6]. While the localized surface plasmon resonances of individual nanoparticles suffer from dephasing and dissipative losses, periodic arrays of such nanoparticles with lattice constants in the order of the wavelength allow to couple the plasmon resonance to the diffractive orders of the lattice, giving rise to collective surface lattice resonances (SLRs) with reports of quality (Q) factors larger than 2000 at telecom wavelengths [7] and geometry-specific, angle-dependent dispersions [8, 9].

Van der Waals materials are an ideal candidate for adding new functionality to metasurfaces due to their rich optical properties [10], intrinsic two-dimensionality and ease of integration by viscoelastic stamping [11]. Transition metal dichalcogenide (TMD) monolayers are particularly appealing due to direct bandgaps [12, 13], large exciton binding energies [14, 15], high oscillator strengths [16, 17], and valley-selective chiral optical transitions [18–20], with recent demonstrations of resonance tuning of atomically thin lenses [21], separation of valley excitons [22], and strong light-matter coupling with dielectric [23–25] and plasmonic cavities [26–28]. Integrating TMDs with plasmonic nanostructures without compromising the optical quality of the TMD is challenging, since they exhibit a strong sensitivity to strain [29] and dielectric disorder [30] due to their two-dimensional (2D)

nature. Encapsulating TMDs in hBN provides an atomically flat and clean dielectric environment preserving optical quality, characterized by the excitonic linewidth approaching the homogeneous limit [31]. However, such an hBN spacer between the TMD and the plasmonic nanoparticles reduces the strength of the near-field and thus the coupling strength significantly. To date, plasmonic nanostructures were either placed in direct contact with the TMD monolayers without hBN encapsulation [26–28, 32–34] or the TMD monolayers were encapsulated in thin hBN layers and placed on top of the plasmonic nanostructures [35–37]. A fully integrated realization without compromising optical quality or coupling strength in TMD-based plasmonic metasurfaces has remained elusive.

In this work, we demonstrate strong coupling in a TMD-based plasmon-exciton-polariton metasurface with a linearly polarized emission profile, utilizing a novel fabrication method we developed that allows us to embed a gold nanodisk array directly into an hBN layer and thus fully integrate it into a van der Waals metasurface. The excitons in the TMD monolayer are in immediate proximity to the near-field of the plasmonic SLRs, while remaining fully encapsulated in a flat and strain-free environment, resulting in an enhanced light-matter coupling strength. The bright exciton X couples strongly to the SLRs of the plasmonic lattice, giving rise to plasmon-exciton-polaritons with large Rabi splitting. The resulting emission profile of the lower polariton branches is strongly modified with respect to an uncoupled monolayer, showing narrow-angle, directional light emission with linear polarization, characteristic for the SLRs of a square lattice.

Our sample contains a monolayer of WSe₂, synthesized by chemical vapor deposition and encapsulated in hBN.

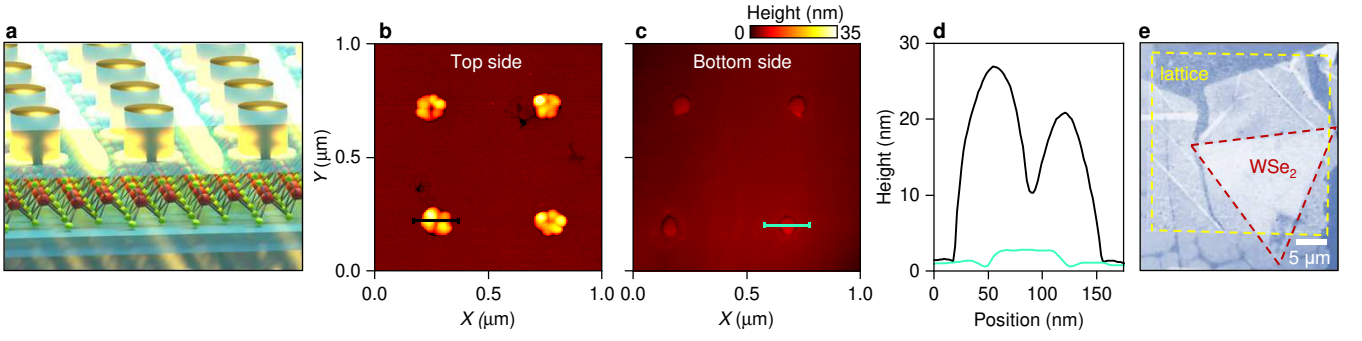


FIG. 1. **Plasmon-exciton-polariton metasurface concept.** **a**, Illustration of the metasurface and the near-field of a plasmonic SLR. The sample consists of a TMD monolayer sandwiched between two hBN flakes, with a gold nanodisk lattice embedded in the top hBN layer. **b** and **c**, Atomic force micrographs of the top and bottom sides of a gold nanodisk array imprinted in hBN. The bottom side was measured with the hBN lattice flake on a PDMS/PCL stamp. **d**, Height profiles of individual gold nanodisks indicated by the black and green lines in **b** and **c**. **e**, False-color optical micrograph of the sample with dashed lines indicating the lattice and the WSe_2 monolayer.

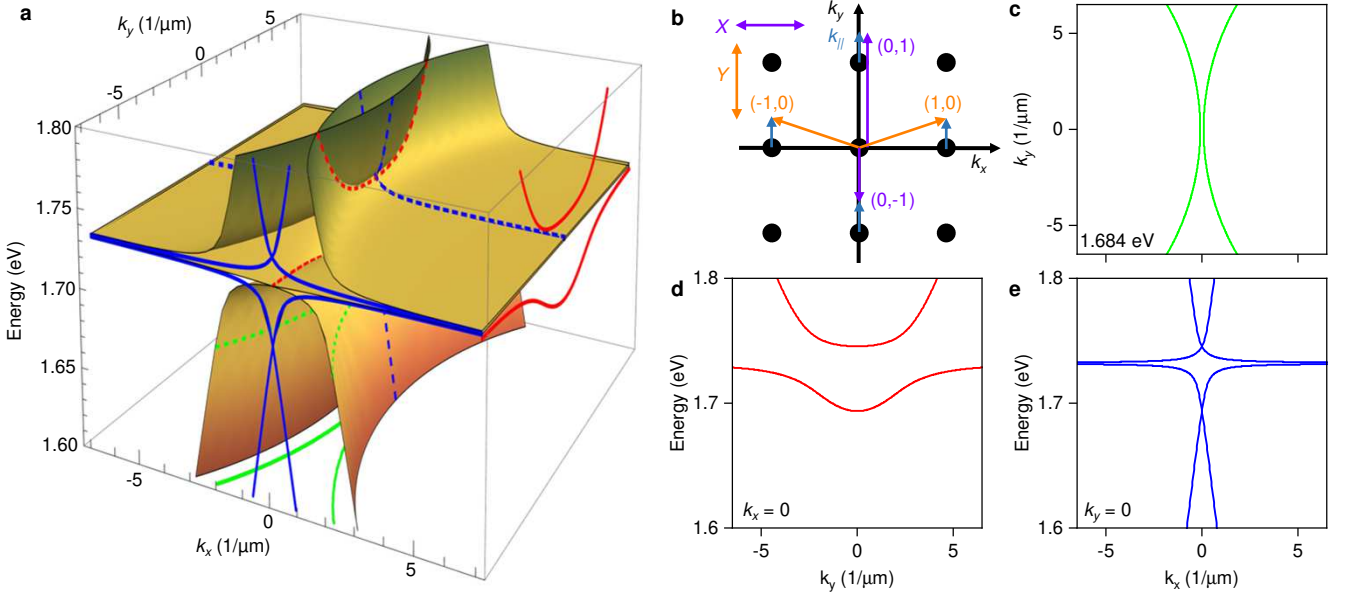


FIG. 2. **Plasmon-exciton-polariton dispersion.** **a**, 3D plot of the plasmon-exciton-polariton energy dispersion [Eq. (1)] of the Y-polarized SLRs with $(\pm 1, 0)$ diffractive orders. **b**, Reciprocal lattice of a square lattice with in-plane k -vector k_{\parallel} along k_y . The four lowest diffractive orders $[(\pm 1, 0)$ and $(0, \pm 1)]$, as well as linear X and Y polarization are indicated. **c** – **e**, 2D projections of the 3D dispersion in **a** with $E = 1.684$ eV (**c**), $k_x = 0$ (**d**), and $k_y = 0$ (**e**).

In the top hBN layer, we incorporated a plasmonic gold nanodisk array by dry-etching air-holes into hBN and filling them with gold (details in Methods), with an illustration of the metasurface shown in Fig. 1a. Atomic force micrographs of the top and bottom sides of the hBN layer with the incorporated gold lattice are shown in Figs. 1b, c and linecuts of the height profiles in Fig. 1d, clearly indicating that the bottom side (roughness < 1 nm) is significantly smoother than the top side, with the additional advantage that it was not directly exposed to any processing. The hBN-gold layer was then transferred on top of the TMD monolayer, providing a flat and clean interface and immediate proximity to the near-field of the

plasmonic SLRs. The robustness of the lattice allows consequent pickup of the TMD monolayer via the hot-pickup technique [11], with an optical micrograph of the heterostructure shown in Fig. 1e.

The SLR dispersions are described with a geometric model of the diffractive orders of the lattice [9], illustrated in Fig. 2b for momentum along the k_y axis (see Methods for details). Strong coupling of the bright exciton X to the plasmonic SLRs gives rise to exciton-polaritons with the energy dispersion of the upper (E_{UP}) and lower (E_{LP}) polariton branches given as (see Meth-

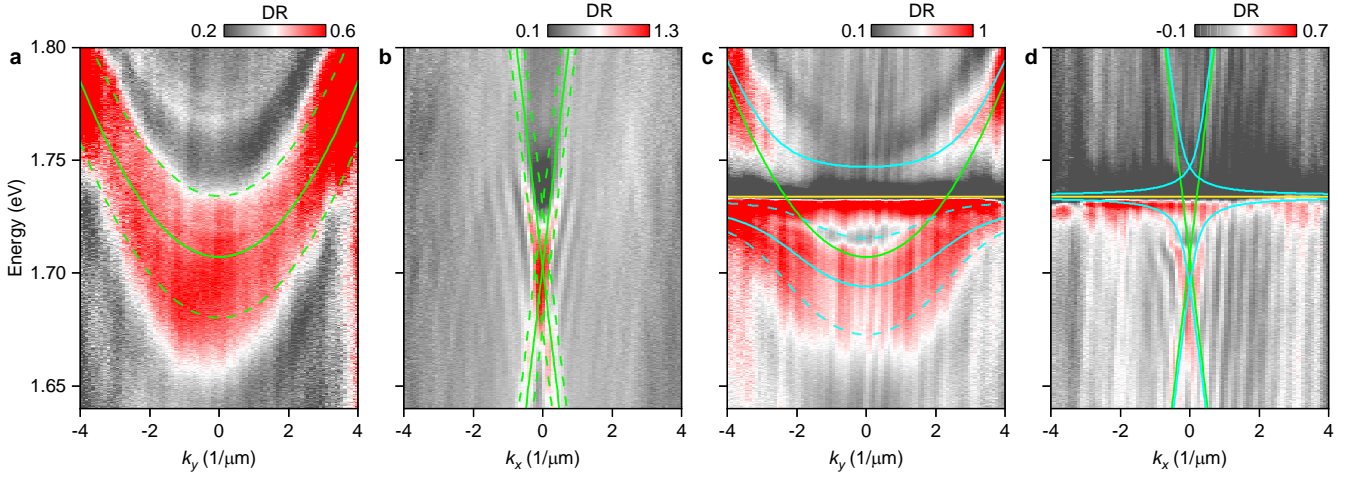


FIG. 3. **Momentum-space dispersions.** **a** and **b**, Hyperbolic and linear dispersions of the $(\pm 1, 0)$ SLRs of the uncoupled lattice in differential reflectance (DR) with linear excitation along Y and detection along k_y and k_x , respectively. Solid (dashed) lines indicate the fitted dispersions (linewidth of $\gamma_{\text{SLR}} = 27$ meV). **c** and **d**, DR polariton dispersions with linear excitation along Y and detection along k_y and k_x , respectively. The SLRs (green), exciton energy (yellow), and fitted polariton branches (cyan) are overlaid. Dashed cyan lines in **c** indicate the lower polariton linewidth γ_{LP} . The light-matter coupling strength g is 25 meV.

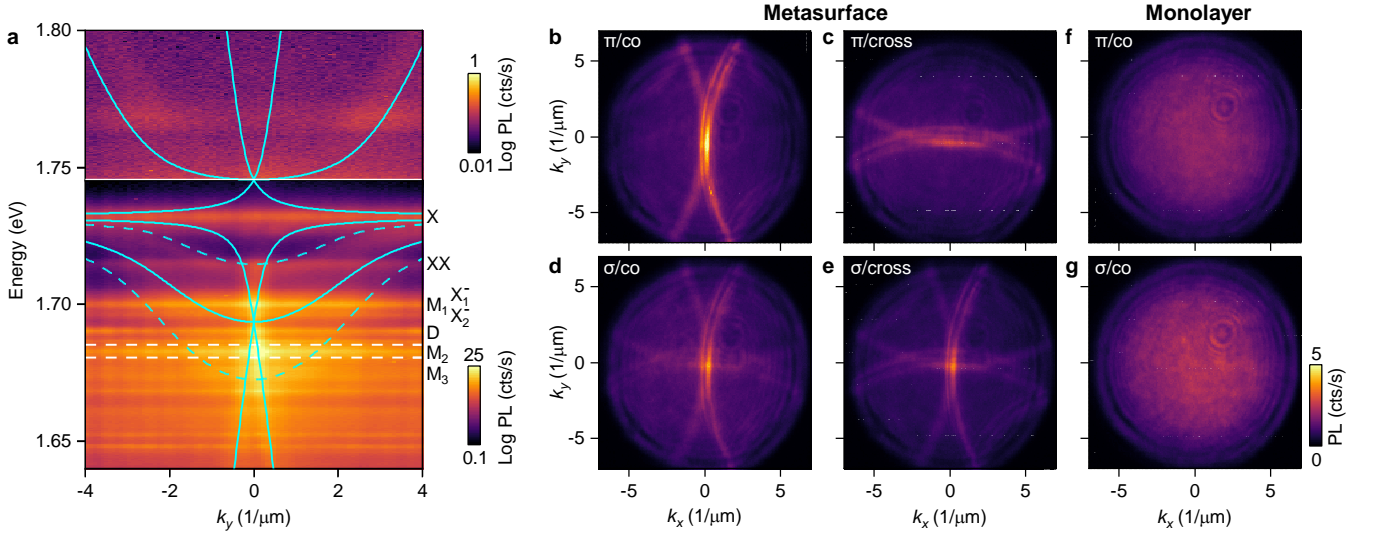


FIG. 4. **Momentum-space photoluminescence.** **a**, PL polariton dispersion with linear excitation along Y ; $E_{\text{LP,UP}}$ (solid cyan) and γ_{LP} (dashed cyan) for the hyperbolic dispersion are indicated. The top and bottom parts of the dispersion have different intensity scales to better visualize E_{UP} . **b** – **e** Momentum-space PL images of the linearly polarized lower polariton branches on the metasurface in the energy range indicated by white dashed lines in **a**. The excitation was linear along Y (π) or circular (σ) and the detection was co- or cross-polarized, indicated in each panel. **f** and **g**, Same as **b** and **d** but on a bare WSe_2 monolayer with Gaussian emission profile.

ods for details):

$$E_{\text{UP,LP}}(k_x, k_y) = \frac{E_{\text{SLR}} + E_{\text{X}} - i(\gamma_{\text{X}} - \gamma_{\text{SLR}})}{2} \pm \sqrt{g^2 - \frac{1}{4}[E_{\text{X}} - E_{\text{SLR}} - i(\gamma_{\text{X}} - \gamma_{\text{SLR}})]^2}, \quad (1)$$

where E_{X} (E_{SLR}) and γ_{X} (γ_{SLR}) are the exciton (SLR) energy and half-width at half-maximum linewidth, respectively, and g denotes the light-matter coupling

strength. A three-dimensional (3D) plot of the upper and lower polariton branches formed by the Y -polarized $(\pm 1, 0)$ diffractive orders is shown in Fig. 2a, and the corresponding 2D projections in Figs. 2c – e.

Using momentum-resolved differential reflectance (DR) spectroscopy, we first studied the $(\pm 1, 0)$ SLRs on the bare lattice with Y -polarized broad-band excitation and detection along k_y (k_x), shown in Fig. 3a (Fig. 3b). The SLR dispersions, fitted with Eq. (2) in Methods,

are degenerate hyperbolic (Fig. 3a) or non-degenerate linear (Fig. 3b), depending on the combination of excitation and detection axes, and show a linewidth of $\gamma_{\text{SLR}} = 27$ meV, much narrower than for localized surface plasmons at the same energy [37], corresponding to a Q factor of 32. In the metasurface region, we observe an avoided crossing and the formation of the upper and lower polariton branches (Figs. 3c, d). By fitting Eq. (1), we extracted $g = 25 \pm 2$ meV and obtained a Rabi splitting Ω_R of 44 ± 5 meV (see Methods for details), much larger than previously reported for polaritons in a TMD monolayer coupled to a dielectric metasurface [25]. Our sample clearly fulfills the common criteria for strong coupling, $g > |\gamma_X - \gamma_{\text{SLR}}|/2$ and $\Omega_R > \gamma_X + \gamma_{\text{SLR}}$ [38, 39], with $\gamma_X = 3.5$ meV.

To probe the emission characteristics, we studied the sample in momentum-resolved photoluminescence (PL) spectroscopy (Fig. 4a). The WSe₂ monolayer spectrum is known to be rich: in addition to X and its upper and lower polariton branches, we observe two dipolar transitions red-shifted from X by 19 and 43 meV, labeled as XX and D, which are the biexciton [40–43] and spin-forbidden dark exciton [44, 45], respectively. A series of peaks labeled M₁ through M₃ also overlap in energy with the lower polariton branches. The assignment of M₁ at 33 meV red-shift remains ambiguous, with direct PL emission from momentum-indirect KK' [46–48] or a phonon sideband of KK' excitons [49] as possible origins. Around M₁ is the negative trion doublet X_1^- and X_2^- with 6 meV exchange splitting [50], visible in our sample due to residual doping. M₂ and M₃, at 50 and 59 meV red-shift have been assigned to phonon sidebands of momentum-indirect KK' excitons [46, 47].

We chose a narrow energy range around M₂ (1.683 ± 0.002 eV) because this phonon sideband does not have any oscillator strength, as it arises from exciton-phonon coupling without any direct absorption or emission of photons, and thus cannot couple to the SLRs, and performed polarization-resolved momentum-space imaging (Figs. 4b – g). Under linear excitation and co-polarized detection, we observe a linearly polarized, directional far-field emission profile from the metasurface (Fig. 4b), with part of the emission constrained to small angles (going from 2° at $k_y = 0$ up to 12° at maximum k_y). For cross-polarized detection, we observe the same signature but rotated by 90° (Fig. 4c). Under circularly polarized excitation and detection, both sets of linear branches are observed simultaneously (Figs. 4d, e). In contrast, on a bare monolayer, the emission profile is Gaussian (Figs. 4f, g), as expected for excitons with out-of-plane dipolar emission profile [51]. The directional narrow-angle emission of the metasurface is a clear signature of the lower polariton branches (cf. Fig. 2c).

The degrees of linear (P_L) and circular (P_C) polarization, determined from polarization resolved PL as $P_{L/C} = (I_{\text{co}} - I_{\text{cross}})/(I_{\text{co}} + I_{\text{cross}})$, where $I_{\text{co/cross}}$ are the co/cross-polarized PL intensities, are shown in Fig. 5. The bright exciton X in monolayer WSe₂ (Figs. 5a, b)

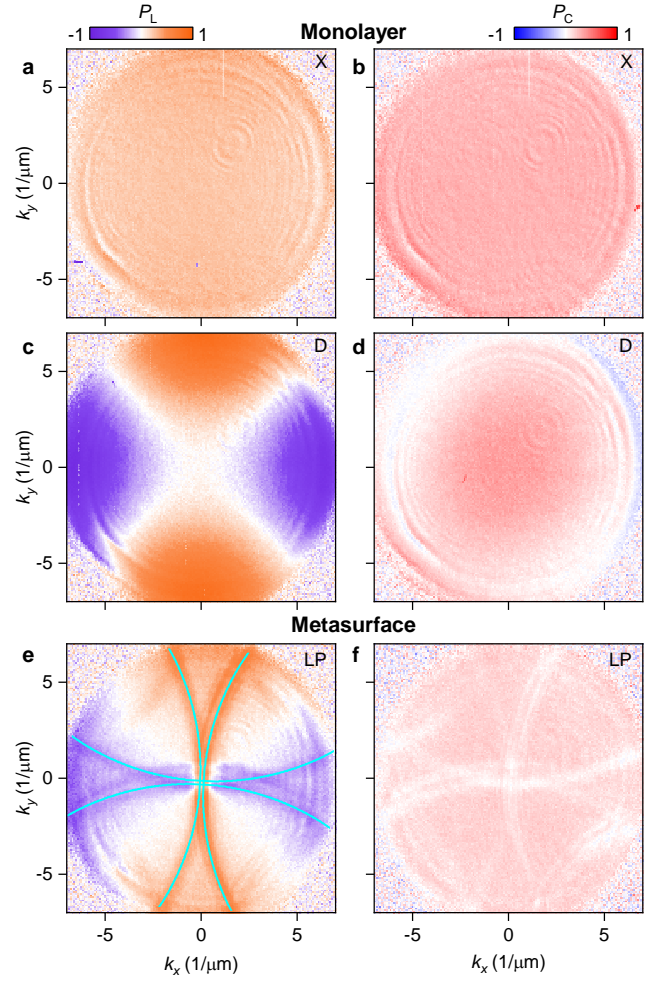


FIG. 5. **Degree of polarization in the far-field.** a and b, Degrees of linear polarization P_L and circular polarization P_C of the bright exciton X in a WSe₂ monolayer with an in-plane polarized optical dipole and out-of-plane emission. c and d, P_L and P_C of the dark exciton D in the monolayer with an out-of-plane polarized optical dipole with in-plane emission. e and f, P_L and P_C of the linearly polarized lower polariton branches of the metasurface, with cyan lines in e indicating the fitted dispersions of the lower polariton branches corresponding to the four lowest diffractive orders.

shows both positive P_L and P_C due to valley-coherence and valley-polarization, respectively [19, 52–54]. The dark exciton D has an out-of-plane polarized optical dipole with in-plane emission [51], showing zero P_L and finite P_C at small k and large P_L and zero P_C at large k (Fig. 5c, d). In contrast, the lower polariton shows large P_L up to 60% and near zero P_C along the branches of its dispersions (Figs. 5e, f), effectively imprinting the polarization of the plasmonic lattice onto the WSe₂ monolayer via strong coupling.

In conclusion, we have demonstrated strong coupling and a linearly polarized emission profile in a TMD-based metasurface using a novel fabrication method. We integrated a gold plasmonic lattice directly into an hBN

layer, preserving dielectric encapsulation of the TMD, while providing immediate proximity to the near-field of the plasmonic SLRs, resulting in enhanced coupling strength and good optical quality, characterized by narrow exciton linewidths. We demonstrated polaritons with a Rabi splitting of 44 ± 5 meV and a strongly modified emission profile. The far-field emission profile showed narrow-angle, directional, linearly-polarized lower polariton branches. The linear polarization of the square plasmonic lattice is imprinted onto the TMD via strong coupling, effectively quenching its intrinsic circular polarization. The polarization and emission profiles can be tuned by using different lattice geometries. Employing chiral nanostructures instead of disks would enhance the valley polarization of the TMD monolayer with applications in opto-valleytronics [55–57].

I. METHODS

A. Sample fabrication

High-quality WSe_2 monolayers were synthesized by in-house chemical vapor deposition, and hBN flakes were exfoliated from bulk crystals (NIMS). We fabricated gold nanodisk arrays embedded in hBN by employing electron-beam lithography (EBL) and inductively-coupled plasma (ICP) etching. A square array of 70 nm diameter nanodisks was defined via EBL using PMMA 950 K resist with a thickness of around 200 nm and a dose of $500 \mu\text{C}/\text{cm}^2$. Air-holes were etched into the hBN via ICP. The plasma was fed by 5 sccm of Ar and 10 sccm of SF_6 at a constant chamber pressure of 10 mTorr. Setting the ICP power to 70 W and the RF power to 6 W yielded a controlled etch rate of 0.6 nm/s. After etching, a gold film matching the thickness of the hBN layer was deposited via electron-beam evaporation. The hardened resist was lifted-off in acetone and isopropanol, and remaining residues were removed in an O_2 asher.

A common figure of merit for etched nanostructures is the sidewall verticality, with efforts invested in achieving vertical nanostructures in hBN [58–60]. Reactive ion etching and electron-beam induced etching were used to create almost vertical sidewalls [59], while a single ICP step achieved etch verticality up to 80° in micron-scale structures with very high etch rates [58]. In this work, we achieved a sidewall angle of around 60° with a good control over the etch time, yielding 70 nm diameter holes, and consequently nanodisks, with flat bottom sides. While the disk shape on the top side is influenced by the sidewall inclination, the bottom side showed a roughness below 1 nm, as highlighted in Figs. 1b – d.

For the design of the gold nanodisk array, we used the finite-difference time-domain method (software Lumerical). The resonance width of SLRs does not depend strongly on the lattice geometry [61]. We designed the structures as gold disks organized on a square lattice with a lattice constant of 480 nm, disk diameters of 70 nm, and

a height of 42 nm (matching the hBN thickness). We then selected the thickness of the second hBN layer such that the simulated resonance energy matched the energy of the bright exciton X in monolayer WSe_2 .

For transfer, we used a dry stamping method with a polydimethylsiloxane (PDMS) droplet on a glass slide as stamp base, which we covered with a thin film of poly-bisphenol A-carbonate (PC, Sigma Aldrich) or polycaprolactone (PCL, Sigma Aldrich). We created the PC (PCL) film by dispersing a solution of polymer dissolved in chloroform (tetrahydrofuran, THF) at a mass percentage of 8% (15%). A 4 nm bottom hBN flake was picked up with a PC stamp at 50°C , released onto a glass substrate at 195°C , and cleaned in chloroform, acetone, and isopropanol. For the pick-up of the hBN flake with the incorporated gold lattice, a PCL stamp was used. We started the process at 30°C and heated up to 57°C to cover the entire flake with the stamp. At this temperature just below its melting point (60°C), PCL becomes viscous and highly sticky [62]. After cooling back down to 30°C , we lifted the flake with embedded lattice off the substrate and released it onto a WSe_2 monolayer at 75°C , followed by cleaning in THF, acetone, and isopropanol. Then a PC stamp was used to pick up the stack at 115°C , followed by release onto the bottom hBN flake at 195°C . The sample was cleaned in chloroform, acetone, and isopropanol and annealed in ultrahigh vacuum for 15 h at 200°C to remove trapped air and residues.

B. Optical spectroscopy

Cryogenic DR and PL spectroscopy were performed in back-scattering geometry in a closed-cycle cryostat (attocube systems, attoDRY800) with 4 K base temperature. To position the sample with respect to a low temperature apochromatic objective (LT-APO/633-RAMAN/0.81), we used piezo-units (attocube systems, ANPx101, ANPz101, and ANSxy100). Angle-resolved DR and PL spectra were recorded with a lab-built Fourier imaging setup in 4f and telescope configuration employing four achromatic doublet lenses (Edmund Optics, VIS-NIR with focal lengths of 750, 750, 400 and 150 mm) and including a dove prism to rotate the Fourier image. The signal was dispersed by a monochromator (Teledyne Princeton Instruments, IsoPlane SCT320), with a 300 grooves/mm grating and detected by a Peltier-cooled (Teledyne Princeton Instruments, PIXIS 1024) charge-coupled device (CCD). Narrow-energy momentum-space images were recorded by turning two tunable filters (Semrock 790 nm VersaChrome Edge tunable Shortpass and Longpass Filters) and by moving the spectrometer grating to zero order and opening the slit. The conversion of camera pixel to wavevector in $1/\mu\text{m}$ was obtained via the size of the illuminated area on the CCD and using the relation $k_{\parallel} = k_0 \sin(\Theta)$ with the maximum angle Θ given by the numerical aperture of the objective, and $k_0 = 2\pi/\lambda$. For both DR and PL measurements, we used

a pulsed supercontinuum laser (NKT Photonics, SuperK with Varia). DR was defined as $DR = (R - R_0)/R_0$, where R was the reflectance from the sample and R_0 was the reference reflectance from a region containing only hBN. PL was excited near the WSe₂ 2s resonance (first higher excited state of X in the exciton Rydberg series [63]) at 662 ± 5 nm and $20 \mu\text{W}$.

C. SLR and polariton dispersions

The SLR dispersions are described by a geometric model of the diffractive orders of the lattice [9], illustrated in Fig. 2b. The k -vector of the SLRs is given by $k_{\text{SLR}} = k_{\text{DO}} + k_{\parallel}$ and their energy by:

$$E_{\text{SLR}}(k_x, k_y) = \frac{\hbar c}{n_{\text{eff}}} \sqrt{\left(\frac{2n\pi}{a} + k_x\right)^2 + \left(\frac{2m\pi}{a} + k_y\right)^2}, \quad (2)$$

with lattice constant a , diffractive orders (n, m) , and effective refractive index n_{eff} . At $k = 0$, $\lambda_{\text{SLR}} \approx n_{\text{eff}}a$. By fitting Eq. (2) to the dispersions measured at different positions on the uncoupled lattice over an area of $378 \mu\text{m}^2$, we determined an average $n_{\text{eff}} = 1.517 \pm 0.007$, corresponding to $E_{\text{SLR}} = 1.70 \pm 0.01$ eV at $k = 0$. We determined the SLR half-width at half-maximum linewidth as $\gamma_{\text{SLR}} = 27$ meV by fitting a Gaussian at $k = 0$ in phase-corrected (with Kramers-Kronig relation) DR. Under linearly polarized excitation, light couples either to the $(\pm 1, 0)$ or $(0, \pm 1)$ diffractive orders, which show degenerate hyperbolic or non-degenerate linear energy dispersions depending on the combination of linear polarization and k -space detection axes.

In the metasurface region, we observe exciton-polariton formation. We fit a coupled oscillator model [27, 64] with the Hamiltonian:

$$H = \begin{pmatrix} E_X - i\gamma_X & g \\ g & E_{\text{SLR}} - i\gamma_{\text{SLR}} \end{pmatrix}. \quad (3)$$

Diagonalization yields the well-known energy relation for the upper and lower polariton branches given by Eq. (1) in the main text. By fitting Eq. (1) to the dispersions measured at different positions over an area of

$306 \mu\text{m}^2$ of the metasurface with $\gamma_X = 3.5$ meV (determined by Lorentzian fitting of the phase-corrected DR on a monolayer region) and $\gamma_{\text{SLR}} = 27$ meV, we extracted $g = 25 \pm 2$ meV, $n_{\text{eff}} = 1.513 \pm 0.005$, and $E_X = 1.731 \pm 0.003$ eV.

The Rabi splitting Ω_R is defined as [39]:

$$\Omega_R = 2\sqrt{g^2 - \frac{1}{4}(\gamma_X - \gamma_{\text{SLR}})^2}, \quad (4)$$

and is 44 ± 5 meV. The linewidth of the lower polariton branch is given by [65]:

$$\gamma_{\text{LP}} = |X|^2\gamma_X + |C|^2\gamma_{\text{SLR}}, \quad (5)$$

where X and C are the Hopfield coefficients [39]:

$$|X|^2 = \frac{1}{2} \left[1 + \frac{E_{\text{SLR}} - E_X}{\sqrt{\Omega_R^2 + (E_{\text{SLR}} - E_X)^2}} \right], \quad (6)$$

$$|C|^2 = \frac{1}{2} \left[1 - \frac{E_{\text{SLR}} - E_X}{\sqrt{\Omega_R^2 + (E_{\text{SLR}} - E_X)^2}} \right], \quad (7)$$

and shown as dashed cyan lines in Figs. 3c and 4a for the hyperbolic polariton dispersion.

Author Information

Corresponding authors:

F. T.-V. (f.tabataba@lmu.de) and A. H. (alexander.hoegel@lmu.de).

Author Contributions:

F. T.-V. and L. K. contributed equally to this work.

Notes:

The authors declare no competing financial interest.

Acknowledgements: This research was funded by the European Research Council (ERC) under the Grant Agreement No. 772195 and the Deutsche Forschungsgemeinschaft (DFG, German Research Foundation) within Germany's Excellence Strategy under grant No. EXC-2111-390814868. F. T.-V. acknowledges funding from the Munich Center for Quantum Science and Technology (MCQST) and the European Union's Framework Programme for Research and Innovation Horizon Europe under the Marie Skłodowska-Curie Actions grant agreement No. 101058981. K. W. and T. T. acknowledge support from the JSPS KAKENHI (Grant Numbers 20H00354 and 23H02052) and World Premier International Research Center Initiative (WPI), MEXT, Japan.

-
- [1] N. Yu and F. Capasso, Flat optics with designer metasurfaces, *Nat. Mater.* **13**, 139 (2014).
 [2] N. Meinzer, W. L. Barnes, and I. R. Hooper, Plasmonic meta-atoms and metasurfaces, *Nat. Photonics* **8**, 889 (2014).
 [3] H.-T. Chen, A. J. Taylor, and N. Yu, A review of metasurfaces: physics and applications, *Rep. Prog. Phys.* **79**,

076401 (2016).

- [4] N. Yu, P. Genevet, M. A. Kats, F. Aieta, J.-P. Tetienne, F. Capasso, and Z. Gaburro, Light propagation with phase discontinuities: generalized laws of reflection and refraction, *Science* **334**, 333 (2011).
 [5] L. Huang, X. Chen, H. Mühlender, H. Zhang, S. Chen, B. Bai, Q. Tan, G. Jin, K.-W. Cheah, C.-W. Qiu, J. Li,

- T. Zentgraf, and S. Zhang, Three-dimensional optical holography using a plasmonic metasurface, *Nat. Commun.* **4**, 2808 (2013).
- [6] F. Aieta, P. Genevet, M. A. Kats, N. Yu, R. Blanchard, Z. Gaburro, and F. Capasso, Aberration-free ultrathin flat lenses and axicons at telecom wavelengths based on plasmonic metasurfaces, *Nano Lett.* **12**, 4932 (2012).
- [7] S. Deng, R. Li, J.-E. Park, J. Guan, P. Choo, J. Hu, P. J. Smeets, and T. W. Odom, Ultranarrow plasmon resonances from annealed nanoparticle lattices, *Proc. Natl. Acad. Sci. U.S.A.* **117**, 23380 (2020).
- [8] C. Cherqui, M. R. Bourgeois, D. Wang, and G. C. Schatz, Plasmonic surface lattice resonances: Theory and computation, *Acc. Chem. Res.* **52**, 2548 (2019).
- [9] R. Guo, T. K. Hakala, and P. Törmä, Geometry dependence of surface lattice resonances in plasmonic nanoparticle arrays, *Phys. Rev. B* **95**, 155423 (2017).
- [10] Y. Meng, H. Zhong, Z. Xu, T. He, J. S. Kim, S. Han, S. Kim, S. Park, Y. Shen, M. Gong, Q. Xiao, and S.-H. Bae, Functionalizing nanophotonic structures with 2D van der Waals materials, *Nanoscale Horiz.* **8**, 1345 (2023).
- [11] F. Pizzocchero, L. Gammelgaard, B. S. Jessen, J. M. Caridad, L. Wang, J. Hone, P. Bøggild, and T. J. Booth, The hot pick-up technique for batch assembly of van der Waals heterostructures, *Nat. Commun.* **7**, 11894 (2016).
- [12] A. Splendiani, L. Sun, Y. Zhang, T. Li, J. Kim, C.-Y. Chim, G. Galli, and F. Wang, Emerging photoluminescence in monolayer MoS₂, *Nano Lett.* **10**, 1271 (2010).
- [13] K. F. Mak, C. Lee, J. Hone, J. Shan, and T. F. Heinz, Atomically thin MoS₂: a new direct-gap semiconductor, *Phys. Rev. Lett.* **105**, 136805 (2010).
- [14] K. He, N. Kumar, L. Zhao, Z. Wang, K. F. Mak, H. Zhao, and J. Shan, Tightly bound excitons in monolayer WSe₂, *Phys. Rev. Lett.* **113**, 026803 (2014).
- [15] A. Chernikov, T. C. Berkelbach, H. M. Hill, A. Rigosi, Y. Li, B. Aslan, D. R. Reichman, M. S. Hybertsen, and T. F. Heinz, Exciton binding energy and nonhydrogenic Rydberg series in monolayer WS₂, *Phys. Rev. Lett.* **113**, 076802 (2014).
- [16] C. Zhang, H. Wang, W. Chan, C. Manolatou, and F. Rana, Absorption of light by excitons and trions in monolayers of metal dichalcogenide MoS₂: Experiments and theory, *Phys. Rev. B* **89**, 205436 (2014).
- [17] Y. Li, A. Chernikov, X. Zhang, A. Rigosi, H. M. Hill, A. M. Van Der Zande, D. A. Chenet, E.-M. Shih, J. Hone, and T. F. Heinz, Measurement of the optical dielectric function of monolayer transition-metal dichalcogenides: MoS₂, MoSe₂, WS₂, and WSe₂, *Phys. Rev. B* **90**, 205422 (2014).
- [18] D. Xiao, G.-B. Liu, W. Feng, X. Xu, and W. Yao, Coupled spin and valley physics in monolayers of MoS₂ and other group-VI dichalcogenides, *Phys. Rev. Lett.* **108**, 196802 (2012).
- [19] K. F. Mak, K. He, J. Shan, and T. F. Heinz, Control of valley polarization in monolayer MoS₂ by optical helicity, *Nat. Nanotechnol.* **7**, 494 (2012).
- [20] G. Wang, A. Chernikov, M. M. Glazov, T. F. Heinz, X. Marie, T. Amand, and B. Urbaszek, Colloquium: Excitons in atomically thin transition metal dichalcogenides, *Rev. Mod. Phys.* **90**, 021001 (2018).
- [21] J. Van de Groep, J.-H. Song, U. Celano, Q. Li, P. G. Kik, and M. L. Brongersma, Exciton resonance tuning of an atomically thin lens, *Nat. Photonics* **14**, 426 (2020).
- [22] L. Sun, C.-Y. Wang, A. Krasnok, J. Choi, J. Shi, J. S. Gomez-Diaz, A. Zepeda, S. Gwo, C.-K. Shih, A. Alù, and X. Li, Separation of valley excitons in a MoS₂ monolayer using a subwavelength asymmetric groove array, *Nat. Photonics* **13**, 180 (2019).
- [23] S. Dufferwiel, S. Schwarz, F. Withers, A. Trichet, F. Li, M. Sich, O. Del Pozo-Zamudio, C. Clark, A. Nalitov, D. Solnyshkov, G. Malpuech, K. S. Novoselov, J. M. Smith, M. S. Skolnick, D. N. Krizhanovskii, and A. I. Tartakovskii, Exciton-polaritons in van der Waals heterostructures embedded in tunable microcavities, *Nat. Commun.* **6**, 8579 (2015).
- [24] X. Liu, T. Galfsky, Z. Sun, F. Xia, E.-c. Lin, Y.-H. Lee, S. Kéna-Cohen, and V. M. Menon, Strong light-matter coupling in two-dimensional atomic crystals, *Nat. Photonics* **9**, 30 (2015).
- [25] Y. Chen, S. Miao, T. Wang, D. Zhong, A. Saxena, C. Chow, J. Whitehead, D. Gerace, X. Xu, S.-F. Shi, and A. Majumdar, Metasurface integrated monolayer exciton polariton, *Nano Lett.* **20**, 5292 (2020).
- [26] W. Liu, B. Lee, C. H. Naylor, H.-S. Ee, J. Park, A. C. Johnson, and R. Agarwal, Strong exciton-plasmon coupling in MoS₂ coupled with plasmonic lattice, *Nano Lett.* **16**, 1262 (2016).
- [27] S. Wang, Q. Le-Van, F. Vaianella, B. Maes, S. Eizagirre Barker, R. H. Godiksen, A. G. Curto, and J. Gomez Rivas, Limits to strong coupling of excitons in multilayer WS₂ with collective plasmonic resonances, *ACS Photonics* **6**, 286 (2019).
- [28] W. Liu, Y. Wang, B. Zheng, M. Hwang, Z. Ji, G. Liu, Z. Li, V. J. Sorger, A. Pan, and R. Agarwal, Observation and active control of a collective polariton mode and polaritonic band gap in few-layer WS₂ strongly coupled with plasmonic lattices, *Nano Lett.* **20**, 790 (2019).
- [29] Z. Khatibi, M. Feierabend, M. Selig, S. Brem, C. Linderälrv, P. Erhart, and E. Malic, Impact of strain on the excitonic linewidth in transition metal dichalcogenides, *2D Mater.* **6**, 015015 (2018).
- [30] A. Raja, L. Waldecker, J. Zipfel, Y. Cho, S. Brem, J. D. Ziegler, M. Kulig, T. Taniguchi, K. Watanabe, E. Malic, T. F. Heinz, T. C. Berkelbach, and A. Chernikov, Dielectric disorder in two-dimensional materials, *Nat. Nanotechnol.* **14**, 832 (2019).
- [31] F. Cadiz, E. Courtade, C. Robert, G. Wang, Y. Shen, H. Cai, T. Taniguchi, K. Watanabe, H. Carrere, D. Lagarde, M. Manca, T. Amand, P. Renucci, S. Tongay, X. Marie, and B. Urbaszek, Excitonic linewidth approaching the homogeneous limit in MoS₂-based van der Waals heterostructures, *Phys. Rev. X* **7**, 021026 (2017).
- [32] S. Wang, S. Li, T. Chervy, A. Shalabney, S. Azzini, E. Orgiu, J. A. Hutchison, C. Genet, P. Samori, and T. W. Ebbesen, Coherent coupling of WS₂ monolayers with metallic photonic nanostructures at room temperature, *Nano Lett.* **16**, 4368 (2016).
- [33] J. Sun, Y. Li, H. Hu, W. Chen, D. Zheng, S. Zhang, and H. Xu, Strong plasmon-exciton coupling in transition metal dichalcogenides and plasmonic nanostructures, *Nanoscale* **13**, 4408 (2021).
- [34] C. Guo, J. Yu, and S. Deng, Hybrid metasurfaces of plasmonic lattices and 2D materials, *Adv. Funct. Mater.* **33**, 2302265 (2023).
- [35] M. Klein, B. H. Badada, R. Binder, A. Alfrey, M. McKie, M. R. Koehler, D. G. Mandrus, T. Taniguchi, K. Watanabe, B. J. LeRoy, and J. R. Schaibley, 2D semiconductor nonlinear plasmonic modulators, *Nat. Commun.* **10**, 3264

- (2019).
- [36] A. M. Dibos, Y. Zhou, L. A. Jauregui, G. Scuri, D. S. Wild, A. A. High, T. Taniguchi, K. Watanabe, M. D. Lukin, P. Kim, and H. Park, Electrically tunable exciton-plasmon coupling in a WSe₂ monolayer embedded in a plasmonic crystal cavity, *Nano Lett.* **19**, 3543 (2019).
- [37] S. Vadia, J. Scherzer, K. Watanabe, T. Taniguchi, and A. Högele, Magneto-optical chirality in a coherently coupled exciton-plasmon system, *Nano Lett.* **23**, 614 (2023).
- [38] D. G. Baranov, M. Wersall, J. Cuadra, T. J. Antosiewicz, and T. Shegai, Novel nanostructures and materials for strong light-matter interactions, *ACS Photonics* **5**, 24 (2018).
- [39] C. Schneider, M. M. Glazov, T. Korn, S. Höfling, and B. Urbaszek, Two-dimensional semiconductors in the regime of strong light-matter coupling, *Nat. Commun.* **9**, 2695 (2018).
- [40] Y. You, X.-X. Zhang, T. C. Berkelbach, M. S. Hybertsen, D. R. Reichman, and T. F. Heinz, Observation of biexcitons in monolayer WSe₂, *Nat. Phys.* **11**, 477 (2015).
- [41] M. Barbone, A. R.-P. Montblanch, D. M. Kara, C. Palacios-Berraquero, A. R. Cadore, D. De Fazio, B. Pingault, E. Mostaani, H. Li, B. Chen, K. Watanabe, T. Taniguchi, S. Tongay, G. W. amd Andrea C. Ferrari, and M. Atatüre, Charge-tuneable biexciton complexes in monolayer WSe₂, *Nat. Commun.* **9**, 3721 (2018).
- [42] Z. Li, T. Wang, Z. Lu, C. Jin, Y. Chen, Y. Meng, Z. Lian, T. Taniguchi, K. Watanabe, S. Zhang, D. Smirnov, and S.-F. Shi, Revealing the biexciton and trion-exciton complexes in BN encapsulated WSe₂, *Nat. Commun.* **9**, 3719 (2018).
- [43] A. Steinhoff, M. Florian, A. Singh, K. Tran, M. Kolarczik, S. Helmrich, A. W. Achtstein, U. Woggon, N. Owschimikow, F. Jahnke, and X. Li, Biexciton fine structure in monolayer transition metal dichalcogenides, *Nat. Phys.* **14**, 1199 (2018).
- [44] X.-X. Zhang, Y. You, S. Y. F. Zhao, and T. F. Heinz, Experimental evidence for dark excitons in monolayer WSe₂, *Phys. Rev. Lett.* **115**, 257403 (2015).
- [45] C. Robert, T. Amand, F. Cadiz, D. Lagarde, E. Courtade, M. Manca, T. Taniguchi, K. Watanabe, B. Urbaszek, and X. Marie, Fine structure and lifetime of dark excitons in transition metal dichalcogenide monolayers, *Phys. Rev. B* **96**, 155423 (2017).
- [46] M. He, P. Rivera, D. Van Tuan, N. P. Wilson, M. Yang, T. Taniguchi, K. Watanabe, J. Yan, D. G. Mandrus, H. Yu, H. Dery, W. Yao, and X. Xu, Valley phonons and exciton complexes in a monolayer semiconductor, *Nat. Commun.* **11**, 618 (2020).
- [47] E. Liu, J. van Baren, C.-T. Liang, T. Taniguchi, K. Watanabe, N. M. Gabor, Y.-C. Chang, and C. H. Lui, Multipath optical recombination of intervalley dark excitons and trions in monolayer WSe₂, *Phys. Rev. Lett.* **124**, 196802 (2020).
- [48] M. Yang, L. Ren, C. Robert, D. Van Tuan, L. Lombez, B. Urbaszek, X. Marie, and H. Dery, Relaxation and darkening of excitonic complexes in electrostatically doped monolayer WSe₂: Roles of exciton-electron and trion-electron interactions, *Phys. Rev. B* **105**, 085302 (2022).
- [49] J. Förste, N. V. Tepliakov, S. Y. Kruchinin, J. Lindlau, V. Funk, M. Förg, K. Watanabe, T. Taniguchi, A. S. Baimuratov, and A. Högele, Exciton g-factors in monolayer and bilayer WSe₂ from experiment and theory, *Nat. Commun.* **11**, 4539 (2020).
- [50] E. Courtade, M. Semina, M. Manca, M. Glazov, C. Robert, F. Cadiz, G. Wang, T. Taniguchi, K. Watanabe, M. Pierre, W. Escoffier, E. L. Ivchenko, P. Renucci, X. Marie, T. Amand, and B. Urbaszek, Charged excitons in monolayer WSe₂: Experiment and theory, *Phys. Rev. B* **96**, 085302 (2017).
- [51] G. Wang, C. Robert, M. M. Glazov, F. Cadiz, E. Courtade, T. Amand, D. Lagarde, T. Taniguchi, K. Watanabe, B. Urbaszek, and X. Marie, In-plane propagation of light in transition metal dichalcogenide monolayers: optical selection rules, *Phys. Rev. Lett.* **119**, 047401 (2017).
- [52] H. Zeng, J. Dai, W. Yao, D. Xiao, and X. Cui, Valley polarization in MoS₂ monolayers by optical pumping, *Nat. Nanotechnol.* **7**, 490 (2012).
- [53] A. M. Jones, H. Yu, N. J. Ghimire, S. Wu, G. Aivazian, J. S. Ross, B. Zhao, J. Yan, D. G. Mandrus, D. Xiao, W. Yao, and X. Xu, Optical generation of excitonic valley coherence in monolayer WSe₂, *Nat. Nanotechnol.* **8**, 634 (2013).
- [54] G. Wang, X. Marie, B. Liu, T. Amand, C. Robert, F. Cadiz, P. Renucci, and B. Urbaszek, Control of exciton valley coherence in transition metal dichalcogenide monolayers, *Phys. Rev. Lett.* **117**, 187401 (2016).
- [55] S.-H. Gong, F. Alpegiani, B. Sciacca, E. C. Garnett, and L. Kuipers, Nanoscale chiral valley-photon interface through optical spin-orbit coupling, *Science* **359**, 443 (2018).
- [56] G. Hu, X. Hong, K. Wang, J. Wu, H.-X. Xu, W. Zhao, W. Liu, S. Zhang, F. Garcia-Vidal, B. Wang, P. Lu, and C.-W. Qiu, Coherent steering of nonlinear chiral valley photons with a synthetic Au-WS₂ metasurface, *Nat. Photonics* **13**, 467 (2019).
- [57] S. Guddala, R. Bushati, M. Li, A. Khanikaev, and V. Menon, Valley selective optical control of excitons in 2D semiconductors using a chiral metasurface, *Opt. Mater. Express* **9**, 536 (2019).
- [58] S. Grenadier, J. Li, J. Lin, and H. Jiang, Dry etching techniques for active devices based on hexagonal boron nitride epilayers, *J. Vac. Sci. Technol. A* **31** (2013).
- [59] J. E. Fröch, Y. Hwang, S. Kim, I. Aharonovich, and M. Toth, Photonic nanostructures from hexagonal boron nitride, *Adv. Opt. Mater.* **7**, 1801344 (2019).
- [60] L. Kühner, L. Sortino, B. Tilmann, T. Weber, K. Watanabe, T. Taniguchi, S. A. Maier, and A. Tittl, High-Q nanophotonics over the full visible spectrum enabled by hexagonal boron nitride metasurfaces, *Adv. Mater.* **35**, 2209688 (2023).
- [61] A. D. Humphrey and W. L. Barnes, Plasmonic surface lattice resonances on arrays of different lattice symmetry, *Phys. Rev. B* **90**, 075404 (2014).
- [62] S. Son, Y. J. Shin, K. Zhang, J. Shin, S. Lee, H. Idzuchi, M. J. Coak, H. Kim, J. Kim, J. H. Kim, M. Kim, D. Kim, P. Kim, and J.-G. Park, Strongly adhesive dry transfer technique for van der Waals heterostructure, *2D Mater.* **7**, 041005 (2020).
- [63] A. V. Stier, N. P. Wilson, K. A. Velizhanin, J. Kono, X. Xu, and S. A. Crooker, Magneto-optics of exciton Rydberg states in a monolayer semiconductor, *Phys. Rev. Lett.* **120**, 057405 (2018).
- [64] L. Shi, T. Hakala, H. Rekola, J.-P. Martikainen, R. Møerland, and P. Törmä, Spatial coherence properties of organic molecules coupled to plasmonic surface lattice resonances in the weak and strong coupling regimes, *Phys.*

Rev. Lett. **112**, 153002 (2014).

- [65] H. Deng, H. Haug, and Y. Yamamoto, Exciton-polariton Bose-Einstein condensation, Rev. Mod. Phys. **82**, 1489 (2010).